Mapping microscope object polarized emission to the back focal plane pattern

Thomas P. Burghardt
Mayo Clinic Rochester
Department of Biochemistry and Molecular Biology
    and
Department of Physiology and Biomedical Engineering
200 First Street South West
Rochester, Minnesota 55905
E-mail: burghardt@mayo.edu

Katalin Ajtai
Mayo Clinic Rochester
Department of Biochemistry and Molecular Biology
200 First Street South West
Rochester, Minnesota 55905

Abstract. The back focal plane (BFP) intensity pattern from a high-aperture objective separately maps far- and near-field emission from dipoles near a bare glass or metal-film-coated glass/aqueous interface. Total internal reflection (TIR) excitation of a fluorescent sample gave a BFP pattern interpreted in terms of fluorescent dipole orientation and distance from the interface. Theoretical consideration of this system led to identification of emission characteristics that remove a dipole orientation degeneracy in conventional microscope fluorescence polarization measurements. BFP pattern inspection removes the degeneracy. Alternatively, a BFP mask blocking a small fraction of emitted light in a standard imaging microscope prevents uniform collection of the BFP intensity and also eliminates the degeneracy. The BFP pattern from a single photoactivated photoactivatable green fluorescent protein (PAGFP) tagged myosin in a muscle fiber was observed despite the large background light from the highly concentrated myosin tagged with unphotoactivated PAGFP. This was accomplished by imaging the pattern from a nontelecentric plane, where most of the background intensity's pattern was translated laterally from the single-molecule object's pattern. TIR/BFP pattern imaging requires a simple alteration of the fluorescence microscope and is consistent with single-molecule imaging in a fluorophore dense three-dimensional object like a muscle fiber. © *2009 Society of Photo-Optical Instrumentation Engineers.*
[DOI: 10.1117/1.3155520]

1 Introduction

Fluorescent markers are highly sensitive, potentially single-molecule, detectors used in cells, tissues, and other biological specimens. They can identify and characterize low abundance substrates in the visible wavelengths where biological specimens have low autofluorescence and where marker fluorescence is efficiently collected in a microscope objective. They are also direction sensors due to the electric dipole–mediated excitation and fluorescence-coupled decay. The electric dipole is nominally fixed in the molecular frame of the fluorophore that is likewise fixed relative to the substrate. Absorption and fluorescence emission from the dipole is recognized to obey absorption probability and emitted intensity angular distribution rules leading to deduction of probe orientation from collected polarized fluorescence intensities.

The fluorescence microscope is an imaging instrument producing a real image of the fluorescence source at a light detector. Nevertheless, accurate spatial representation of the fluorescent source might be secondary to efficient light detection in some applications although resolution and light detection efficiency tend to improve together with increasing numerical aperture (NA) of the microscope objective. A single-molecule fluorescence polarization application in which the sources are sufficiently separated or selectively activated only needs microscope collection efficiency.[1,2] In this case, an image of the objective back focal plane (BFP) light intensity distribution contains all the dipole orientation information in a pattern that is interpretable by inspection.[3,4]

The fluorescence microscope is an efficient emitted light-collecting instrument that can also perturb the emission intensity angular distribution that we wish to measure. The perturbation is complex in a microscope utilizing total internal reflection excitation (TIR). In TIR microscopy, excitation light impinges on a glass/aqueous interface from the glass side at angles beyond critical angle for TIR. The light totally reflects and remains inside the glass substrate except for an evanescent layer of excitation energy in the aqueous phase that decays exponentially in the direction normal to the interface. The evanescent excitation excites fluorescence from the sample in the aqueous phase in a region within $\sim$100 nm of the interface. At this short distance, the interface alters the emission angular pattern and total emitted energy of the fluo-

rophore as described by Hellen and Axelrod.[5] The interface converts emitter dipole nonpropagating (near-field) into propagating (far-field) energy density collected by the high-NA objective. Additionally, the high-NA collecting lens intermingles emitter linear polarization components again predictably perturbing the emission angular pattern.[6] To varying degrees, both effects enrich the information content of the BFP pattern and complicate its quantitative interpretation.

Here we describe efforts to calculate and observe the two-dimensional BFP emission pattern for a high-NA microscope objective. Patterns were observed under TIR illumination of bare glass/aqueous and glass/thin-aluminum-film/aqueous interfaces. Samples observed included fluorescent nanospheres and single photoactivatable green fluorescent proteins (PAGFP) tagged myosin light chains exchanged onto myosin cross-bridges in skeletal muscle fibers. The latter is an interesting biological application on crowded proteins, where emission from a single brightly fluorescent probe competes with background from many more probes in the low-fluorescence state.[2] Our results show good agreement between observed and calculated patterns for the fluorescent nanosphere sample where sample intensity dominates the pattern. In contrast, while single photoactivated PAGFPs in the muscle fiber sample create a distinctive image even while embedded in background from unphotoactivated PAGFPs, the BFP pattern for the photoactivated PAGFP is much less distinctive. By collecting the BFP pattern at a nontelecentric plane, we can partially separate the single-molecule BFP pattern from the background BFP pattern. The latter method made possible a qualitative interpretation of probe dipole orientation and has potential for further development.

2 Methods

2.1 Chemicals

Carboxylate-modified fluorescent microspheres were purchased from Molecular Probes (Eugene, Oregon). Adenosine triphosphate (ATP), dithiothreitol (DTT), and phenylmethanesulfonyl fluoride (PMSF) were from Sigma Chemical (St. Louis, Missouri). All chemicals were analytical grade or ultrapure, if available.

2.2 Solutions

Rigor solution contains 10 mM imidazole, 2.5 mM ethylene glycol bis(β-aminoethyl ether)-N,N,N$'$,N$'$-tetraacetic acid, 2.2 mM Mg acetate, 130 mM potassium propionate, 0.2 mM PMSF, 0.8 μg/mL leupeptin, and 1 mM DTT.

2.3 Sample Preparations

Rabbit psoas muscle fibers were prepared, and the native myosin regulatory light chain (RLC) exchanged with PAGFP-tagged human cardiac RLC (HCRLC-PAGFP) as described.[1,2]

Red-orange carboxylate-modified fluorescent spheres had 40 nm diam and excitation/emission maxima at 565/580. Sphere concentrations were computed using the formula from the manufacturer and diluted in rigor buffer. We used 10^8-fold dilutions from stock giving sphere concentration of 1.4×10^{19} spheres/mL. All experiments were conducted at room temperature.
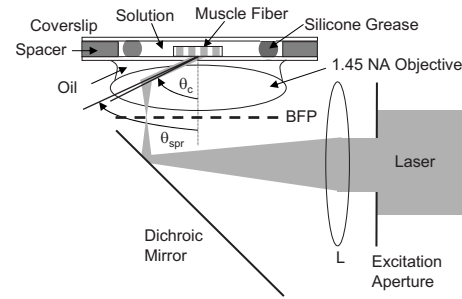

Fig. 1 Lens L focuses 488 or 514 nm of light from an argon-ion laser at the BFP of a 1.45 NA oil-immersion objective. The light is incident from the glass side of the glass/aqueous or glass/metal-film/aqueous interface at angles greater than critical angle, $\theta_c \approx 61.6$ deg, or equal to the surface plasmon resonance angle, $\theta_{spr} \approx 64.6$ deg. The excitation aperture reduces the illuminated area in the sample plane.

2.4 Coverslip Preparation

Clean No. 1 glass coverslips were sonicated for 10 min in ethanol then plasma cleaned (Harrick Plasma, Ithaca, New York) for 15–30 min. Plasma-cleaned coverslips were ready for use in the bare glass interface experiments. Plasma-cleaned coverslips were also thin aluminum (Al) film coated by thermal vacuum evaporation at the Mayo Electron Microscope Facility. In some instances, film deposition was limited to half of the coverslip's top surface by partially covering one coverslip with another during vacuum evaporation. The result was an abrupt edge to the film as viewed in the light microscope. Aluminum film depth was measured with atomic force microscopy by scanning the tip over the edge in the partially aluminized coverslip. Aluminum film depth was estimated to be 20–30 nm.

2.5 Sample Chamber Preparation

Bare glass or Al-coated coverslips were placed on a (1 $\times$ 3)-in. brass slide with a large hole cut out, permitting the objective from the inverted microscope to contact the coverslip through immersion oil. The Al-coated coverslips had the metal side up. A watertight chamber was constructed on top of the coverslip as described.[7] The chamber contained either a suspension of nanospheres or a muscle fiber. Nanospheres settled from suspension onto the coverslip, where some of them adsorbed strongly enough to remain after washing out free nanospheres with rigor buffer. Adsorbed spheres were often aggregates with varying emitted intensities. BFP images were from microsphere aggregates.

2.6 TIR Fluorescence BFP Microscopy

The inverted microscope (Olympus IX71) setup was described previously.[1] Excitation 488 or 514 nm light from an argon-ion laser is focused on the BFP of a 1.45-NA objective and incident from the glass side of a glass/aqueous interface at angles greater than critical angle for TIR, $\theta_c \approx 61.6$ deg (see Fig. 1). Although light is totally reflected, an evanescent field created in the water medium and decaying exponentially with distance from the interface, excites fluorophores within $\sim$100 nm of the surface.[8] The p-polarized incident light has electric field polarization in the incidence plane and produces an elliptically polarized evanescent electric field. Evanescent
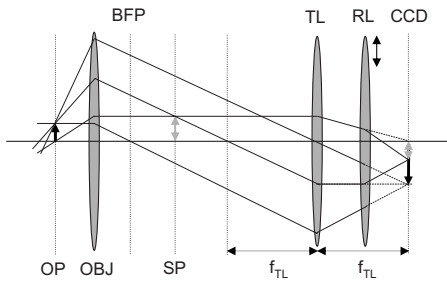
Fig. 2 Optical setup for conventional and BFP pattern imaging. The object (black arrow) is at the object plane (OP), OBJ is objective, SP is the plane where the BFP pattern (double arrow) is observed, TL is tube lens, RL is a removable lens, CCD is the image plane for the camera, and f_{TL} is the tube lens focal length. Light emitted by the object at OP emerges from the back of the objective in parallel rays. RL is removable (bidirectional arrow) to facilitate BFP (RL in) or object (RL out) imaging.

Fig. 3 Far- and near-field emission from dipole μ transmits the interface and propagates into the glass medium at angles beyond critical angle, θ_c, for the dielectric interface or at the SPR angle, θ_{spr}, for the metal-coated interface. SAF is supercritical angle fluorescence referring to any near-field light that propagates into the region defined by $\theta > \theta_c$. The objective lens drawn subtends a solid angle appropriate for a NA=1.45 objective. The BFP and laser beam for TIR excitation are also shown.

intensity is predominantly polarized normal to the interface.[9] The s-polarized incident light has electric field polarization perpendicular to the incidence plane that is continuous across the interface. In the presence of the metal film, the laser penetrates the interface and creates an evanescent field only when incident at the surface plasmon resonance angle, $\theta_{spr} \approx 64.6$ deg (see Fig. 1). P-polarized incident light penetrates the interface while s-polarized light is mostly reflected. Experiments with green fluorescent protein (GFP)-tagged muscle fibers use reduced illumination area on the fiber surface accomplished with the laser diameter reducing aperture shown in Fig. 1.

Fluorescent spheres or HCRLC-PAGFP exchanged muscle fibers in aqueous buffer solution make contact with the TIR-supporting glass or metal-film substrate and are illuminated by the evanescent field. Excited fluorescence is collected by the objective and spectrally filtered using a rhodamine (fluorescent spheres) or fluorescein (GFP-tagged fibers) filter set. Figure 2 shows the optical setup.

The BFP lies within the Olympus objective and is not readily accessible, hence, we image the intensity pattern at the BFP from a sample plane (SP) between the BFP and tube lens (TL). Imaging an object at SP (light double arrow) rather than the BFP changes the image size at the CCD plane. SP is not telecentric, implying an object displaced laterally changes the position of its intensity pattern at SP (the pattern at a telecentric plane is not translated when the object moves laterally). All experiments were conducted with the object at the center of the field. A single molecule from a muscle fiber was centered in the field, but most of the background fluorescence was intentionally displaced from the center likewise displacing its BFP pattern at SP. The background BFP pattern displacement enhances our ability to separately identify BFP patterns for the single molecule and background. The removable lens (RL) is positioned to form a real image of SP at the CCD plane by placing a translucent ruler at SP and adjusting RL position until a real image of it is formed at the CCD plane. The RL is conveniently removable (indicated in Fig. 2 by the two-directional arrow) to facilitate conversion between BFP and normal imaging.
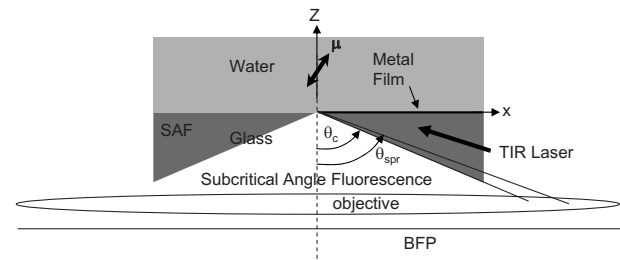
2.7 Emission Near an Interface

When a dipolar is near a conducting or dielectric planar interface, the radiated fields are significantly altered.[5] An emitting fluorophore has a dipolar emission field that is the superposition of propagating transverse waves forming the far-field and nonpropagating longitudinal (evanescent) waves forming the near field. The near field is not detected unless perturbed by a nearby interface creating detectable propagating transverse waves. Converted near-field propagating waves appear in the glass medium at angles beyond θ_c for the dielectric interface or at θ_{spr} for the metal-coated interface. We refer to either emission mode as supercritical angle fluorescence (SAF).[10] Oil immersion objectives with NA $\gtrsim 1.3$ capture SAF. Subcritical angle fluorescence (UAF) is from far-field emission. Figure 3 shows emission near a bare glass (left) or metal-film (right) interface and indicates the critical angle, θ_c, and surface plasmon resonance (SPR) angle, θ_{spr}. The objective lens subtends a polar angle appropriate for a NA=1.45 objective.

The interface also affects total radiated power. Hellen and Axelrod pointed out that, for a fluorophore under steady illumination, the dissipated power must equal the absorbed power, implying that a fixed power, rather than a fixed amplitude, dipole radiator is the appropriate model for probe emission near an interface.[5] An important consequence of the power normalization is that the metal film totally quenches fluorescence from probes within ~10 nm of the interface. Hellen and Axelrod also pointed out conditions where reflection coefficients for the conducting interface need to incorporate nonlocal effects due to the dipole's near-field coupling to surface waves whose wavelengths do not satisfy the condition of being much greater that the mean free path of conducting electrons in the metal. They use reflection coefficients derived from quasistatic semiclassical infinite barrier (SCIB) theory.[11] The SCIB correction, inserted when large wavenumber radial waves of the dipole's near-field contribute to energy dissipation, is largest for dipoles very near to the metal film ($\lesssim 5$ nm) and affects total power dissipated by the dipole.

The high-NA collection of light in a microscope objective mixes light contributions from emitter dipole Cartesian components due to the collection of light from a large solid angle surrounding the dipole. The Cartesian dipole moments produce differently polarized light that is combined by the objec-
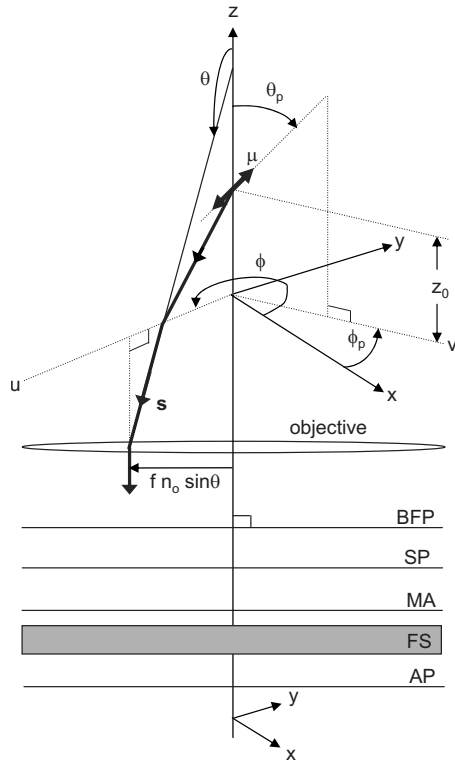
Fig. 4 The spatial relationship of the dipole moment μ, interface (xy plane), objective, BFP, sample plane (SP), pattern mask (MA), filter set (FS), and analyzing polarizer (AP). The bare glass or metal-film-coated glass side of the interface lies in the $z<0$ half-plane and the aqueous side in the $z\geq0$ half-plane. The u- and v-auxiliary lines lie in the xy plane. Dipole μ is at the focal point of the objective with z-axis position z_0 and orientation in the microscope fixed frame given by (θ_p, ϕ_p). Heavy arrows delineate an emitted light ray path. The ray is incident on the objective with propagation vector **s** and emerges in image space at distance $fn_o \sin\theta$ from the z-axis, where f is the objective focal length and n_o is the refractive index for the objective and immersion oil. Coordinates $(fn_o \sin\theta, \phi)$ define the observation point at the BFP or SP.

tive such that their individual contributions cannot be separated using an analyzing polarizer. Separating the contributions into the Cartesian components of the dipole moment is the basis for fluorescence polarization measurement of dipole orientation. Axelrod described the solution to the problem in a homogeneous medium.[6]

We address the probe emission perturbation by the interface and the complications for polarized light collection by a high NA objective in the dipolar emission intensity from single probes. Our computations give the two-dimensional intensity pattern in the objective BFP for comparison to experiment and show the effect of probe orientation on the pattern.

Computation and display of BFP intensity patterns were performed using software written for Mathematica (version 6.0, Wolfram Research, Champaign, Illinois).

3 Results

3.1 *Two-Dimensional BFP Intensity*

A dipole in aqueous medium near to a bare glass or metal-film-coated glass interface emits light part of which transmits

to the glass side and is collected by the objective. Figure 4 shows the spatial relationship of the dipole moment, interface, objective, BFP, SP, pattern mask (MA), filter set (FS), and analyzing polarizer (AP).

Heavy arrows delineate an emitted light ray path. It leaves the dipole, refracts at the interface and at the objective, then emerges in image space propagating parallel to the z-axis. The ray is incident on the objective with propagation vector **s** and emerges in image space at distance $fn_o \sin\theta$ from the z-axis, where f is the objective focal length and n_o is the objective and immersion-oil refractive index. Coordinates $(fn_o \sin\theta, \phi)$ define the observation point at the BFP. We computed the intensity at SP using the method outlined previously[1] and based on the original work of Hellen and Axelrod.[5]

A fluorescent object translated laterally from the center of the visual field produces the BFP pattern like the centered object implying multiple single molecules in the field produce a summed BFP pattern. The pattern image at SP however is translated with object translation. The translated image is approximated using a coordinate transformation that accounts for the changed light collection geometry but not for the changed light refraction at the objective. The latter would be needed to interpret the translated BFP pattern quantitatively.

An object translated a lateral distance L from at the visual field center is one focus of an ellipse with the other focus at the visual field center. The semimajor axis (a) and eccentricity (e) for the ellipse are

$$a = \left(\frac{1}{2}L + \mathrm{NA}\,f\right) \quad \text{and} \quad e = \frac{L}{2a}. \tag{1}$$

Electric fields computed for the object in (θ', ϕ') coordinates were expressed in coordinates fixed in the visual field center (θ, ϕ) using the following relationships:

$$\tan\phi' = \frac{r\sin\phi}{L + r\cos\phi} \quad r = \frac{a(1-e^2)}{1 + e\cos\phi}$$

$$\tan\left[\theta' - \frac{\pi}{2}\right] = \frac{r\cos[\phi-\phi']\tan\left[\theta - \frac{\pi}{2}\right]}{L\cos\phi' + r\cos[\phi-\phi']} \tag{2}$$

for r the ellipse radius measured from the visual field center focus.

Computed BFP intensity patterns are averaged over square regions to imitate pixilation by a CCD camera. Pixels correspond to 6.45×6.45 μm^2 regions in image space as appropriate for our CCD camera (Hamamatsu, Orca ER).

Figure 5 compares computed BFP intensity patterns for a bare glass interface with a dipole at $z_0=50$ nm and orientation $\theta_p=\pi/3$, and $\phi_p=0$ (top) or π (bottom). Patterns for dipole orientation ϕ_p have a reflection symmetry axis along a line at $\phi=\phi_p$; hence, we can compare patterns with a half-plane representation. All patterns show an intense circular band where critical angle light intersects the BFP (arrows). Light falling outside the band is SAF, and light falling within the band is UAF. Figure 5(a) shows the intensity pattern without the AP. The two dipoles ($\theta_p=\pi/3$ and $\phi_p=0$ or π) are subtly distinguished in the pattern mainly with UAF intensity near the equatorial (horizontal line bisecting the circular pattern). Figures 5(b) and 5(c) show the BFP patterns after analyzing po-
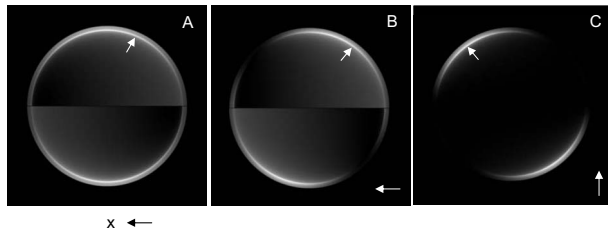
Fig. 5 Computed BFP intensity patterns for a bare glass interface for dipoles at $z_0 = 50$ nm and orientation $\theta_p = \pi/3$, and $\phi_p = 0$ (top), or π (bottom) with x-axis indicated and z-axis pointing into the page. All patterns show an intense circular band where critical angle light intersects the BFP (arrows inside ring). Light falling outside the band is SAF, and light falling within the band is UAF. (A) shows the intensity pattern without the AP. Dipoles with $+x(\phi_p=0)$ and $-x(\phi_p=\pi)$ components (and with $\theta_p = \pi/3$) are distinguished in the pattern mainly with UAF intensity near the equatorial (horizontal line bisecting the circular pattern). (B, C) show the BFP patterns after analyzing polarizer (AP) insertion for active axis at two perpendicular directions indicated by the white arrows in the right bottom corners. The patterns distinguish dipoles equivalent except for the $+x(\phi_p=0)$ and $-x(\phi_p=\pi)$ components in both SAF and UAF intensity. BFP patterns in (A) and (B) differ at 10:30 and 4:30 o'clock where (A) is brighter in the UAF and SAF regions.

larizer (AP) insertion for active axis at two perpendicular directions indicated by the white arrows in the right bottom corners. The patterns distinguish the $\phi_p = 0$ or π dipoles in both SAF and UAF intensity but SAF is the more characteristic indicator of dipole orientation.

The panels demonstrate that an important degeneracy in dipole moment orientation is lifted by BFP imaging. In conventional microscope fluorescence polarization, the dipole orientations (θ_p, ϕ_p), $(\theta_p, \pi+\phi_p)$, and $(\pi-\theta_p, \pi+\phi_p)$ will produce equal intensities. The high-NA objective collects Cartesian dipole component products $\mu_x\mu_y$, $\mu_x\mu_z$, and $\mu_y\mu_z$ in addition to the usual products μ_x^2 and μ_y^2 collected at low NA. The BFP pattern shows the functional dependence on ϕ. The combination (high NA and ϕ dependence in the BFP pattern) removes the (θ_p, ϕ_p), $(\theta_p, \pi+\phi_p)$ degeneracy, but (θ_p, ϕ_p), $(\pi-\theta_p, \pi+\phi_p)$ degeneracy remains. Conventional object imaging microscopy sums intensity uniformly over ϕ reducing to zero weights for the $\mu_x\mu_y$, $\mu_x\mu_z$, and $\mu_y\mu_z$ products thereby removing their contribution from detected intensity. Figure 4 shows the position of the mask within the microscope, which can be configured to nonuniformly sample contributions from different ϕ's reinstating $\mu_x\mu_y$, $\mu_x\mu_z$, and $\mu_y\mu_z$ sensitivity in the total detected intensity. Figure 6 shows angle ϕ and BFP subdivision into four quadrants. Emitted light propagates toward the viewer and the excitation TIR laser beam propagates into the page. Emitted light is blocked from propagating beyond the BFP in the shaded region. The presence of the mask removes the (θ_p, ϕ_p), $(\theta_p, \pi+\phi_p)$ degeneracy. With the mask from Fig. 6, collected intensities for the system depicted in Fig. 5(a) with $(\theta_p, \phi_p) = (\pi/3, 0)$ and $(\pi/3, \pi)$ have relative values of 1 and 0.6, respectively. Under the same circumstances, the intensity ratio for the systems depicted in Figs. 5(b) and 5(c) [the intensity collected in Fig. 5(b) divided by the intensity collected in Fig. 5(c)] is 1 and 2.3 for $(\theta_p, \phi_p) = (\pi/3, 0)$ and $(\pi/3, \pi)$, respectively.
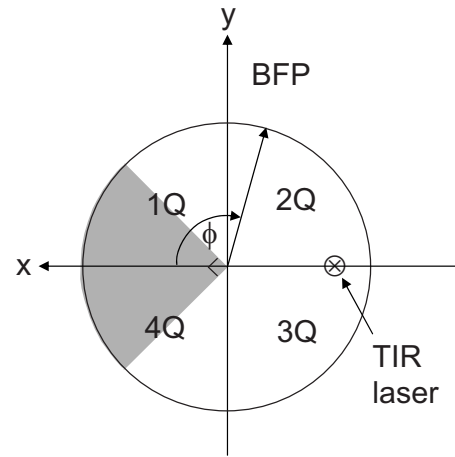

Fig. 6 Variable ϕ and the BFP subdivided into four quadrants of the xy plane. Emitted light propagates toward the viewer and the excitation TIR laser beam propagates into the page. Emitted light is blocked from propagating beyond the BFP in the shaded region.

3.2 *Quantitative BFP Pattern Modeling*

Small aggregates of fluorescent nanospheres were adsorbed onto Al-coated or bare glass coverslips then illuminated under TIR. Figure 7(a) compares experimental (top half) and computed (bottom half) BFP patterns for the nanospheres near the Al-coated interface. The inner ring appears at θ_c (inner arrow, bottom left) position and the outer ring at the θ_{spr} position (outer arrow bottom left).

Figure 7(b) compares experimental and computed patterns showing good alignment of peaks. The parameters needed in the fitting are the dielectric constants for water, glass, and aluminum; the thickness of the metal film d; the distance of the dipole from the interface z_0; and the orientation of the dipole (θ_p, ϕ_p). The dipole orientation was assumed to be perpendicular to the interface $(\theta_p = 0)$ due to the apparent cylindrical symmetry of the rings. We did not investigate other polar angles with cylindrical symmetry imposed by averaging over ϕ_p. Dielectric constants were taken from Ref. 5 while parameters d and z_0 were varied to find a suitable fit.

We find that fitted $d \approx 23$ nm falls within the experimentally determined Al-film depth of 20–30 nm. Fitted dipole position $z_0 \approx 454$ nm is beyond the expected penetration depth of the TIR evanescent field of ~ 100 nm. The discrepancy suggests that the nanosphere aggregate frustrates TIR of the incident beam to propagate excitation into the aggregate.

Figure 8 compares experimental (top half) and computed (bottom half) BFP patterns for the nanospheres aggregate near a bare glass interface. The broad bright ring begins at the critical angle position but continues into the SAF region, indicating probes are emitting very near to the interface. The faint ring patterns seen in the UAF region not reproduced in simulation are probably caused by diffraction of scattered excitation laser light contaminating the image from fluorescence. The same uneven background effect probably produces the faint dark band in the outermost SAF region also not reproduced in simulation. The experimental BFP emission pattern is heterogeneous in ϕ and slightly more intense at the meridian (vertical line bisecting the circular pattern) than at
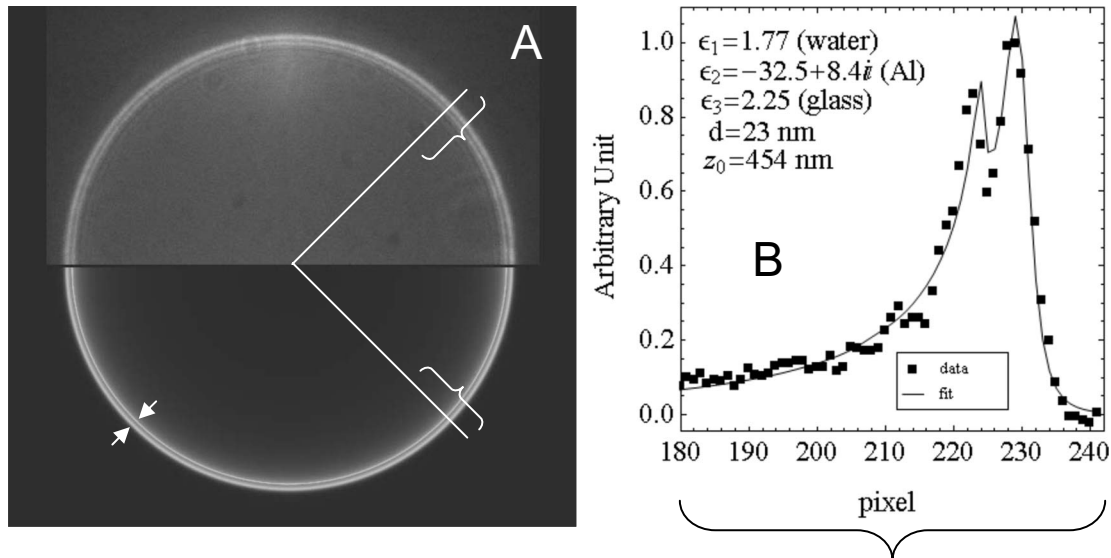
Fig. 7 (A) contains experimental (top half) and computed (bottom half) BFP patterns for nanospheres near the Al-coated interface. The inner ring appears at the critical angle, θ_c, position (inner arrow) and the outer ring at the surface plasmon resonance angle, θ_{spr}, position (outer arrow). (B) compares equivalent projections of the experimental and computed patterns. The computed pattern uses the parameters indicated in (B).

the equatorial line and qualitatively similar to the computed pattern where $(\theta_p, \phi_p) = (\pi/3, \pi)$ and $z_0 = 0$ nm.

Figure 9(a) shows a HCRLC-PAGFP exchanged muscle fiber in rigor at a bare glass interface and under TIR illumination. Emission is dominated by a single photoactivated PAGFP. Background light is from many unphotoactivated HCRLC-PAGFPs in the fiber emitting at ~1% the efficiency of the photoactivated molecule with 488-nm excitation. The exciting TIR laser aperture is closed down (Fig. 1) to minimize the area illuminated around the photoactivated molecule. Further reduction in aperture size unacceptably reduced fluorescence intensity from the photoactivated single molecule. The single dominant photoactivated HCRLC-PAGFP was positioned at the center of the microscope field of view and at the lower edge of the illuminated region such that the majority of background emission originated from the top portion of the field of view.

The right side of Fig. 9(b) shows the BFP image from Fig. 9(a). The left side of Fig. 9(b) shows the simulated BFP image
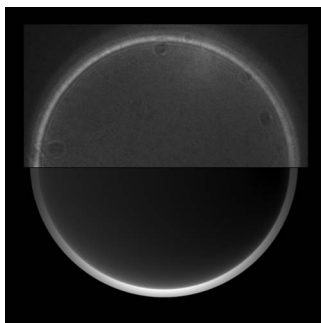
from two objects, one at the center and another translated upward from center of the field of view. An object translated laterally produces a laterally translated BFP image at SP. The object translated upward produces the simulated light ring translated downward in correspondence with the broader ob-
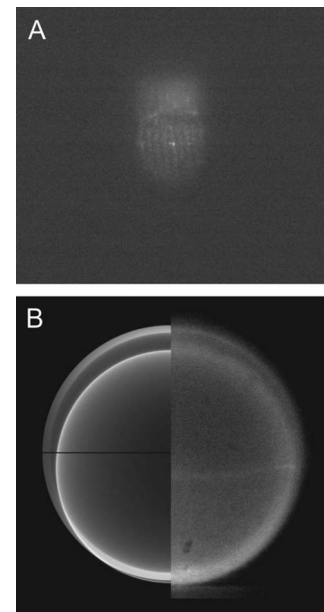

Fig. 8 Experimental (top half) and computed (bottom half) BFP patterns for the nanospheres aggregates near a bare glass interface. The broad bright ring starts at the critical angle, θ_c, and continues into the SAF region indicating probes are emitting very near to the interface. The computed pattern uses $(\theta_p, \phi_p) = (\pi/3, \pi)$ and $z_0 = 0$.

Fig. 9 (A) A HCRLC-PAGFP exchanged muscle fiber in rigor at a bare glass interface and under TIR illumination. The single dominant photoactivated HCRLC-PAGFP is at the center of the microscope field of view and at the lower edge of the illuminated region. (B) The BFP image from (A) and simulated BFP image from an object at the center plus an object translated upward from center of the field of view (right and left hemicircles, respectively). The single dominant photoactivated HCRLC-PAGFP emission in the fiber image maps to the centered ring at the outer edge of the BFP pattern. Background in the fiber image maps to the downward translated broad BFP ring pattern.

served light ring at the BFP. In the fiber image, background is centered upward from the single molecule source but is distributed over the whole illuminated region producing the translated and diffuse light ring in the BFP image. Simulating the distributed background sources over the whole illuminated region is prohibitively computer time consuming and was not attempted.

The object at the center of the field produces the centered simulated light ring in correspondence with the centered observed light ring in the BFP image. The translated background BFP image allows observation of the centered object over about half of the BFP image. The single-molecule source BFP image diminishes at the equator, indicating an oriented single molecule. The simulated ring is identical to that in the lower part of Fig. 5(a), where $(\theta_p, \phi_p) = (\pi/3, \pi)$ and $z_0 = 50$ nm.

4 Discussion

Single fluorescent probe dipole orientation is recognized by its two-dimensional emission pattern at the BFP of a high-NA microscope objective.[3] For the system depicted in Fig. 3 with dipole excited by TIR light, the BFP fluorescence emission pattern has intensity concentrated at the critical angle for the bare glass interface (Fig. 5) and at the critical angle and surface plasmon resonance angle for the thin-metal-film–coated glass interface [Fig. 7(a)]. These distinctive patterns show that a substantial portion of light transmitted into the glass side of the interface is SAF for the bare glass interface and essentially all transmitted emission is SAF and collected into a cone at $\theta_{spr} > \theta_c$ in the presence of the thin metal film. Selecting the objective NA large enough to collect this light is essential for maximizing emitted signal collection efficiency.[4] The θ_{spr} depends on the dielectric constant of the metal film, providing an adjustable parameter to facilitate collection of emitted light. As pointed out by Mattheyses and Axelrod, the θ_{spr} for an Al film is suited for use with the NA = 1.45 TIRF objective.[4]

The BFP pattern from isolated and immobilized single probes determined emitter dipole orientation with good accuracy[3] when compared to alternative emission methods such as defocused orientation imaging[12,13] and other polarization analysis procedures.[12] The BFP patterns distinguish in principal all dipole orientation changes aside from the degeneracy $(\theta_p, \phi_p) \rightarrow (\pi - \theta_p, \pi + \phi_p)$ when the dipole is inverted through the origin. The BFP intensity pattern thus contains dipole orientation information missing from conventional spot intensity fluorescence polarization microscopy. Figure 5(a)–5(c) demonstrate the effect by indicating the ability to distinguish ϕ_p and $\pi + \phi_p$ dipole orientations that are degenerate in conventional microscopy. The degeneracy is lifted because Cartesian dipole component cross products $\mu_x\mu_y$, $\mu_x\mu_z$, and $\mu_y\mu_z$, (where $\mu_x = \sin\theta_p \cos\phi_p$, $\mu_y = \sin\theta_p \sin\phi_p$, and $\mu_z = \cos\theta_p$) are detected (in addition to the usual products μ_x^2 and μ_y^2) with the high-NA objective and the BFP intensity directly shows their effect on the emission pattern. In conventional fluorescence microscopy, the cross products are detected, but this information is lost when the collected intensity is uniformly summed over ϕ. Without BFP pattern information, lost information is recoverable using the mask shown in Figs. 4 and 6. The mask nonuniformly weights contributions

from different ϕ's recovering $\mu_x\mu_y$, $\mu_x\mu_z$, and $\mu_y\mu_z$ sensitivity in the detected intensity.

In muscle, myosin is the actin-dependent molecular motor driving sarcomeric shortening and muscle contraction by transducing chemical free energy from MgATP hydrolysis into directed movement.[14,15] The MgATP hydrolysis is coupled to a series of conformational changes in myosin resulting in the myosin lever arm rotation to impel actin against resistive force.[15] A GFP-tagged myosin light chain (MLC-GFP) was exchanged with the native light chain on the lever arm to fluorescent label the myosin lever arm in a muscle fiber. The MLC-GFP rigidly attaches to the lever arm to detect its rotation with fluorescence polarization.[1]

In the fiber, myosin concentration reaches $120-300~\mu$M,[16,17] implying myosin is crowded and complicating isolation of individual molecules for single-molecule measurements. Recently, photoactivatable GFP-tagged MLC (MLC-PAGFP) was introduced to the fiber.[2] Sparse photoactivation of the PAGFP permitted detection of single-lever-arm orientation in the myosin dense muscle fiber. A persistent difficulty in interpreting fluorescence from the single photoactivated MLC-PAGFP–tagged myosin is background light from many unphotoactivated MLC-PAGFPs in the fiber emitting at $\sim 1\%$ the efficiency of the photoactivated molecule. Figure 9(a) shows a single photoactivated MLC-PAGFP on myosin in the muscle fiber. Laser TIR illumination is nominally uniform in the lateral dimension of object space out to the edge formed by the illumination aperture (Fig. 1), where it drops off rapidly. We reduced background light reaching the BFP by minimizing the overall illuminated region and spatially isolated most of the background light in the BFP pattern by placing the single photoactivated molecule at the center of the viewing field but at the edge of the illuminated region. This arrangement led to the BFP pattern shown in Fig. 9(b), where the single-molecule pattern is translated from much of the background light BFP pattern. Total background light is larger than the single-molecule light; nonetheless, about half of the single-molecule BFP pattern is recognized. More background reduction is needed to make the approach quantitative. Introduction of an Al-film at the interface is one proven background reducing approach we are pursuing.[18] Alternatively, the single-molecule image of Fig. 9(a) separates background from signal. The single-molecule image analyzed by standard spot intensity fluorescence polarization, whereas using the emission mask from Fig. 6 will characterize dipole orientation at the resolution level of the BFP pattern albeit without the convenience of recognizing orientation by inspection.

Dipolar fluorescence emission characteristics in homogeneous space are variously affected when the dipole emits near an interface. The effects are caused by interference of incident and reflected emission on the dipole side of the interface, by conversion of the dipole near field into propagating light across the interface, and by normalization of the dipole emission with the total dissipated power. Fluorescence lifetime, radiated power,[5,19,20] and the radiated power angular distribution are all affected by the interface.[5,21,22] The power-normalized dipole emission gave the corrected radiated power angular distribution[5] and lead to the dramatic observation of metal-film quenching of chromophores within a few nanometers of the metal surface.[18,23] The effect of near field on power-normalized emission transmitted into the denser me-

dium for the dielectric (bare) interface, especially when a metal film coats the dielectric, has been transformative in spectroscopy and microscopy. Surface plasmon-coupled emission (SPCE) occurs when a fluorophore is near a metal-coated dielectric interface and causes emission, transmitting the interface to be uniquely polarized and condensed into a narrow cone of light.[24] TIR illumination of the metal-coated interface produces evanescent excitation light due to the SPR effect in the metal.[25] SPR excitation and SPCE together minimize the detection volume and enhance emitted light collection efficiency, both critical in single-molecule isolation and detection.[18,26] BFP pattern imaging in a microscope gives the opportunity to distinguish the various emission modes (UAF, SAF/SPCE), because all are spatially separated in the pattern. The BFP pattern imaging is also consistent with all excitation modes, including TIR and SPR.

5   Conclusions

We have shown that, through the objective, TIR excitation and BFP pattern imaging give interpretable results related to fluorescent dipole orientation and distance from the interface. Theoretical consideration of this system has led to identification of the specific emission characteristics that remove a significant dipole orientation degeneracy found in standard microscope fluorescence polarization measurements. The degeneracy is lifted by inspection of the BFP pattern but can also be removed in a standard microscope by the introduction of a BFP mask that partially blocks some of the emitted light. The BFP pattern from single photoactivated PAGFP-tagged myosin in a muscle fiber was observed despite the large background light from the highly concentrated myosin tagged with unphotoactivated PAGFP. This was accomplished by moving the pattern imaging plane to a nontelecentric plane, where the bulk of the background intensity is translated at a distance related nonlinearly to its lateral distance from the single-molecule object.

References

1. T. P. Burghardt, K. Ajtai, D. K. Chan, M. F. Halstead, J. Li, and Y. Zheng, "GFP tagged regulatory light chain monitors single myosin lever-arm orientation in a muscle fiber," *Biophys. J.* **93**, 2226–2239 (2007).
2. T. P. Burghardt, J. Li, and K. Ajtai, "Single myosin lever-arm orientation in a muscle fiber detected with photoactivatable GFP," *Biochemistry* **48**, 754–765 (2009).
3. M. A. Lieb, J. M. Zavislan, and L. Novotny, "Single-molecule orientations determined by direct emission pattern imaging," *J. Opt. Soc. Am. B* **21**, 1210–1215 (2004).
4. A. Mattheyses and D. Axelrod, "Fluorescence emission patterns near glass and metal-coated surfaces investigated with back focal plane imaging," *J. Biomed. Opt.* **10**, 054007 (2005).
5. E. H. Hellen and D. Axelrod, "Fluorescence emission at dielectric and metal-film interfaces," *J. Opt. Soc. Am. B* **4**, 337–350 (1987).
6. D. Axelrod, "Carbocyanine dye orientation in red cell membrane studied by microscopic fluorescence polarization," *Biophys. J.* **26**, 557–573 (1979).
7. T. P. Burghardt, K. Ajtai, and J. Borejdo, "*In situ* single molecule imaging with attoliter detection using objective total internal reflection confocal microscopy," *Biochemistry* **45**, 4058–4068 (2006).
8. D. Axelrod and G. M. Omann, "Combinatorial microscopy," *Nat. Rev. Mol. Cell Biol.* **7**, 944–952 (2006).
9. T. P. Burghardt and N. L. Thompson, "Evanescent intensity of a focused gaussian light beam undergoing total internal reflection in a prism," *Opt. Eng.* **23**, 62–67 (1984).
10. T. Ruckstuhl and D. Verdes, "Supercritical angle fluorescence (SAF) microscopy," *Opt. Express* **12**, 4246–4254 (2004).
11. G. W. Ford and W. H. Weber, "Electromagnetic interactions of molecules with metal surfaces," *Phys. Rep.* **113**, 195–287 (1984).
12. E. Toprak, J. Enderlein, S. Syed, S. A. McKinney, R. G. Petschek, T. Ha, Y. E. Goldman, and P. R. Selvin, "Defocused orientation and position imaging (DOPI) of myosin V," *Proc. Natl. Acad. Sci. U.S.A.* **103**, 6495–6499 (2006).
13. A. P. Bartko and R. M. Dickson, "Three-dimensional orientations of polymer-bound single molecules," *J. Phys. Chem. B* **103**, 3053–3056 (1999).
14. H. E. Huxley, "The mechanism of muscular contraction," *Science* **164**, 1356–1366 (1969).
15. H. Onishi and M. F. Morales, "A closer look at energy transduction in muscle," *Proc. Natl. Acad. Sci. U.S.A.* **104**, 12714–12719 (2007).
16. C. R. Bagshaw, in *Outline Studies of Biology: Muscle Contraction*, Chapman and Hall, London (1982).
17. B. A. Tikunov, H. L. Sweeney, and L. C. Rome, "Quantitative electrophoretic analysis of myosin heavy chains in single muscle fibers," *J. Appl. Physiol.* **90**, 1927–1935 (2001).
18. T. P. Burghardt, J. E. Charlesworth, M. F. Halstead, J. E. Tarara, and K. Ajtai, "*In situ* fluorescent protein imaging with metal film-enhanced total internal reflection microscopy," *Biophys. J.* **90**, 4662–4671 (2006).
19. W. Lukosz and R. E. Kunz, "Light emission by magnetic and electric dipoles close to a plane dielectric interface. I. total radiated power," *J. Opt. Soc. Am.* **67**, 1607–1614 (1978).
20. K. H. Drexhage, "Interaction of light with monomolecular dye layers," in *Progress in Optics*, E. Wolf, Ed., 163–232, North-Holland Publishing, Amsterdam (1974).
21. W. Lukosz and R. E. Kunz, "Light emission by magnetic and electric dipoles close to a plane dielectric interface. II. radiation patterns of perpendicular oriented dipoles," *J. Opt. Soc. Am.* **67**, 1615–1619 (1978).
22. T. P. Burghardt and N. L. Thompson, "Effect of planar dielectric interfaces on fluorescence emission and detection: evanescent emission with high aperture collection," *Biophys. J.* **46**, 729–738 (1984).
23. R. M. Fulbright and D. Axelrod, "Dynamics of nonspecific adsorption of insulin of etythrocyte membranes," *J. Fluoresc.* **3**, 1–16 (1993).
24. I. Gryczynski, J. Malicka, Z. Gryczynski, and J. R. Lakowicz, "Radiative decay engineering 4. experimental studies of surface plasmon-coupled directional emission," *Anal. Biochem.* **324**, 170–182 (2004).
25. D. Axelrod, "Total internal reflection fluorescence microscopy in cell biology," *Methods Enzymol.* **361**, 1–33 (2003).
26. J. Borejdo, Z. Gryczynski, N. Calander, P. Muthu, and I. Gryczynski, "Application of surface plasmon coupled emission to study of muscle," *Biophys. J.* **91**, 2626–2635 (2006).